ACS OMEGA

http://pubs.acs.org/journal/acsodf

Article

Investigation of Plasmonic-Enhanced Solar Photothermal Effect of Au NR@PVDF Micro-/Nanofilms

Shenyi Ding, Jixiang Zhang,* Cui Liu, Nian Li, Shudong Zhang, Zhenyang Wang,* and Min Xi*

Cite This: *ACS Omega* 2022, 7, 20750−20760

Read Online

ACCESS | Metrics & More | Article Recommendations | Supporting Information

ABSTRACT: Gold nanospheres (Au NSs) and gold nanorods (Au NRs) are traditional noble metal plasmonic nanomaterials. Particularly, Au NRs with tunable longitudinal plasmon resonance from the visible to the near-infrared (NIR) range were suitable for highly efficient photothermal applications due to the extended light-receiving range. In this work, we synthesized Au NRs and Au NSs of similar volumes and subsequently developed them into Au NR/poly(vinylidene fluoride) (PVDF) and Au NS/PVDF nanofilms, both of which exhibited excellent solar photothermal performance evaluated by solar photothermal experiments. We found that the Au NR/PVDF nanofilm showed a higher solar photothermal performance than the Au NS/PVDF nanofilm. Through detailed analysis, such as morphological characterization, optical measurement, and finite element method (FEM) modeling, we found that the plasmonic coupling effects inside the aggregated Au NR nanoclusters contributed to the spectral blue shifts and intensified the photothermal performance. As compared to Au NS/PVDF nanofilms, the Au NR/PVDF nanofilm exhibited a higher efficient light-to-heat conversion rate because of the extended light-receiving range and high absorbance, as a result of the strong plasmonic interactions inside nanoclusters, which was further validated by monochromatic laser photothermal experiments and FEM simulations. Our work proved that the Au NRs have huge potential for plasmonic solar photothermal applications and are envisioned for novel plasmonic applications.

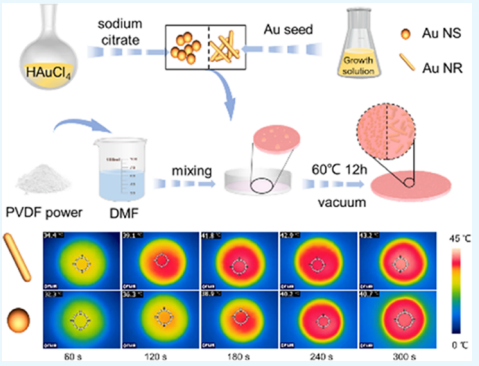

INTRODUCTION

Solar photothermal technology is the most straightforward method to obtain clean energy.[1−3] In general, noble metal nanoparticles like gold and silver, due to their high light-to-heat conversion efficiency,[4] are of interest in photothermal applications,[5] such as in solar steam generation (SSG),[6,7] photoacoustic virus inactivation,[8,9] photothermal therapy,[10] thermal imaging,[11] etc. Noble metal nanoparticles perform photothermal conversion via their localized surface plasmon resonance (LSPR) effects.[12,13] When the irradiated light is in resonance with the nanoparticle's surface plasmon frequency, a portion of light energy will be absorbed and then be transformed in the form of heat as a result of electron−electron and electron−phonon interactions.[14,15]

In the solar radiation spectrum, the solar emission intensive band covers the range from 400 nm to 2.5 μm,[3,16] and the near- to mid-infrared (IR) emissions comprise more than half of the total radiation energy.[17] Therefore, efforts have been made to extend the light-receiving range of the solar photothermal material to optimize the solar energy utilization. Unlike semiconductor plasmonic nanomaterials with adjustable optical properties that usually have near- to mid-IR plasmons,[18−20] noble metal nanoparticle's dipolar plasmon resonance usually tunes its LSPR via its shape.[21−23] As the simplest case, gold nanorods (Au NRs) have independent collective electron oscillations along their transverse or longitudinal directions.[24] Particularly, their longitudinal plasmon can be varied from ∼700 nm in the visible range to 1.2 μm in the near-IR (NIR) range as their aspect ratio (length-to-width ratio) changed from 2.3 to 6.5.[25]

For a complex plasmonic hybridization system (plasmonic molecules), the interactions between individual plasmonic elements (plasmonic atoms) can be attributed to their spectral shifts in the far field and enhancement in the near field.[26] When two nanoparticles approach, with their gap distance being much smaller than their diameters, their dipolar plasmon hybridized and reformed.[27] For example, when two gold nanospheres (Au NSs) approach within the spacing distance (g) much smaller than their diameter (d), their dipolar resonances hybridize and red-shift, and the corresponding spectral shift ($\Delta\lambda$) can be described by the semiempirical equation as a third-order polynomial d^{-3} or exponential functional fits as $\frac{\Delta\lambda}{\lambda} = 0.14\exp\left(\frac{-g/d}{0.23}\right)$.[28] Moreover, if the

Received: February 25, 2022
Accepted: May 25, 2022
Published: June 7, 2022

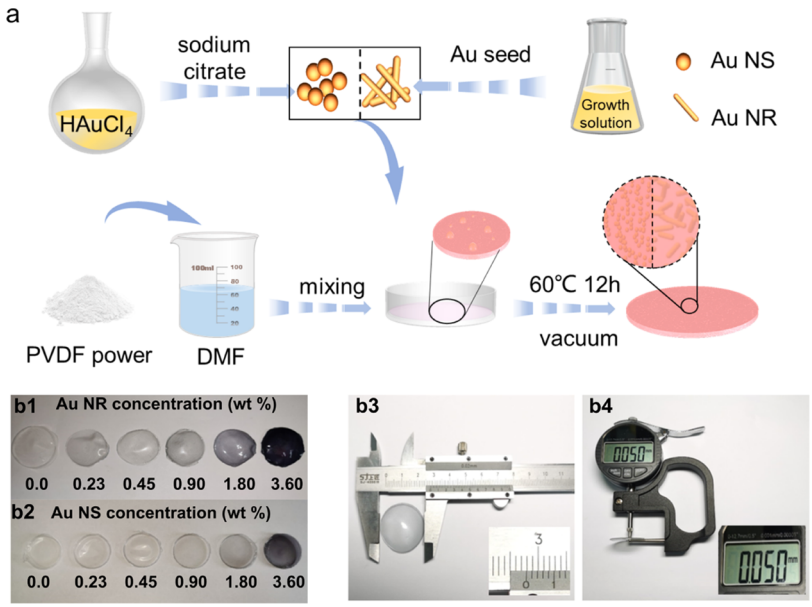

Figure 1. Fabrication of Au NR/PVDF and Au NS/PVDF nanofilms. (a) Scheme depicting the nanofilm fabrication procedure; (b1, b2) photographs of PVDF nanofilms with different Au loading concentrations; and (b3, b4) size measurement of the nanofilm.

close-packed nanoparticles can be assembled into a one-dimensional nanochain, the dipolar resonance along the longitudinal axis can be further tailored into the red with an increased number of nanoparticles or a decreased gap distance, and the corresponding spectral shifts can be described in the form of a semiempirical equation as $\frac{\Delta\lambda}{\lambda_0} = \exp\left(-\frac{m}{x}\right)$,[29,30] where $\Delta\lambda$ is the peak shift ratio defined above, x is the number of chain periods within the chain, m is the characteristic interaction length, and λ_0 is the asymptotic value for the peak shift.

If the gold nanoparticles were assembled into aggregated clusters, the coupled plasmonic interactions inside clusters will lead to both enhanced near- and far-fields. For example, the patterned Au nanoparticle cluster arrays provide an ∼6 times higher Raman signal of the tested bacteria species than the nonpatterned nor aggregated control samples.[31] If additional SiO_2 nanospheres can be well-mixed with Au nanoparticle clusters, the developed Au/SiO_2 photonic-plasmonic nanoarrays will lead to another ∼3 times higher local E-field enhancement factor.[32] Moreover, in the case of the nanofilm composite, the formed coupled plasmonic clusters contribute to the improved light-receiving capability, broaden the light-receiving range, and lead to higher efficient photothermal performance.[7,33] For example, Kyuyoung Bae et al. developed one large-area flexible thin-film black gold membrane consisting of self-aggregated metallic nanowire bundle arrays, which reached an average absorption of 91% under the light-receiving range of 400−2500 nm.[34] Chen et al. developed Au NP/PBONF composite films that can exhibit a solar-vapor conversion efficiency of 83%.[35]

However, the plasmonic coupling of Au NRs is a complicated case because of the formed asymmetric alignment with a higher degree of freedom. Studies have shown that the symmetry-breaking Au NR dimers contribute to their unique near- and far-field optical properties.[36,37] Particularly, the head-to-head (HH) alignment and the shoulder-by-shoulder (SS) alignment are the two most typical cases to start with. For HH alignment, the overall longitudinal dipolar modes are red-shifted, and the "hot spot" region in the gap indicates the near-field coupling, which can be applied to field enhancement molecular sensing applications, such as surface-enhanced Raman scattering (SERS) spectroscopy,[38] surface-enhanced infrared absorption (SEIRA) spectroscopy,[39] surface-enhanced fluorescence emission spectroscopy,[40,41] interference optical sensors,[42] etc. However, for SS alignment, despite the enhanced intensity of the overall transverse mode, the antibonding dark mode can be generated given the condition of asymmetric excitation, which can be used for energy storage applications, such as transformation optics,[43] electromagnetically induced transparency (EIT),[44] Fano resonance,[45] etc. In the cases of bottom-up assembled Au NR nanocomposites, if high surface tension can be generated by an appropriate nanoparticle surfactant and a polymer medium, instead of being uniformly distributed as colloidal suspensions, the nanorods are aggregated into coupled clusters due to surface tension, which are also statistically preferably in SS alignment.[46,47]

Although the spectral shifts of self-assembled or patterned individual Au NR clusters of different azimuthal alignments have been investigated, the aggregated Au NR cluster's coupling effects in the bottom-up assembled nanocomposite in terms of the film's optical response, especially the photothermal performance, to the best of our knowledge, have not been investigated statistically. In this manuscript, we chemically synthesized Au NRs and Au NSs and subsequently developed them into Au NR/poly(vinylidene fluoride) (PVDF) and Au NS/PVDF nanofilms, respectively. The nanoclusters were formed inside the nanofilm via self-assembly due to the surface tension of nanoparticles. Then, we evaluated plasmonic coupling effects of aggregated nanoclusters through morphological characterization, optical measurement, and finite element method (FEM) modeling. Particularly, we found that the formed various styles of Au NR nanoclusters inside the nanofilm contributed to the spectral blue shifts and increased the optical density of the nanofilm. Compared to Au NS/PVDF nanofilms, the Au NR/PVDF nanofilm exhibited a higher efficient light-to-heat conversion rate because of the

https://doi.org/10.1021/acsomega.2c01146
ACS Omega 2022, 7, 20750−20760

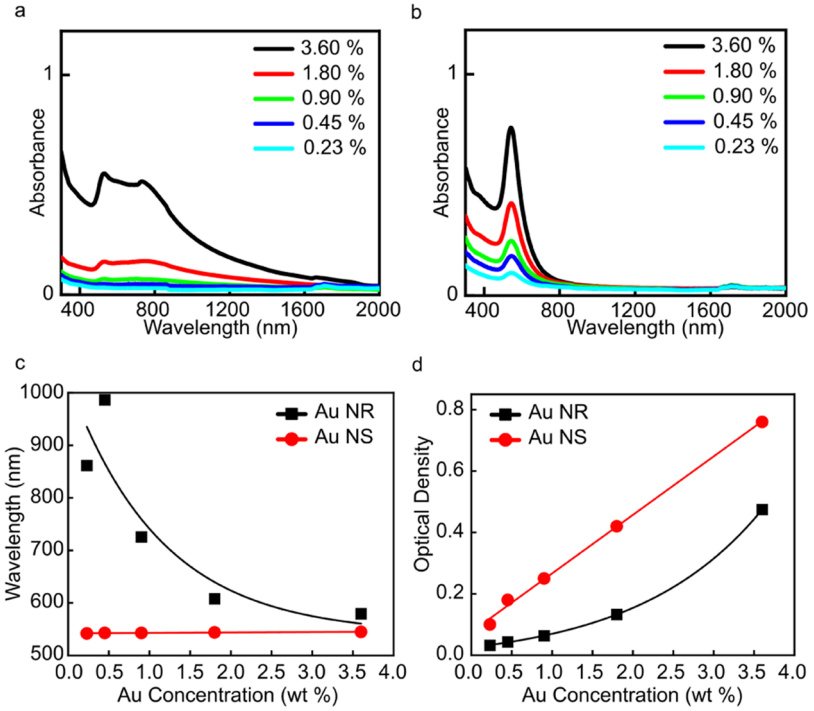

Figure 2. Nanofilm optical characterization. (a, b) UV−vs−NIR spectrum of Au NR/PVDF and Au NS/PVDF nanofilms with different Au loading concentrations; (c) centered absorption wavelength of Au NR/PVDF (black line) and Au NS/PVDF nanofilms (red line) with different Au loading concentrations; and (d) optical density of Au NR/PVDF (black line) and Au NS/PVDF (red line) nanofilms with different Au loading concentrations.

extended light-receiving range and higher absorbance, as a result of plasmonic coupling effects of the nanoclusters. Furthermore, we performed monochromatic laser photothermal experiments and FEM simulations to validate our assumption. Our work proved that the Au NRs have huge potential for plasmonic solar photothermal applications and are promising for a vast range of novel plasmonic applications, such as nanomedicine, tumor treatment, bioimaging, energy storage, etc.

RESULTS AND DISCUSSION

The synthesized Au NRs and Au NSs were examined with transmission electron microscopy (TEM, jem-2100F) for morphological characterization. Figure 1a, b shows the typical TEM images of Au NRs and Au NSs, respectively. In addition, the statistical counts of their size distributions are summarized in Figures S1a1, S1a2, and S1b after processing the images with Nano Measure software. The averaged dimensions of Au NR were 68.9 ± 15.0 nm in length and 8.1 ± 1.0 nm in width with an aspect ratio of ∼8.0. The averaged diameter of Au NS is 18.8 ± 6.0 nm. Based on these measured dimensions, each individual Au NR and Au NS nanoparticle was estimated to have approximately similar volumes as 3468.32 and 3451.46 nm^3, respectively.

We characterized the optical properties of the synthesized colloidal Au NR and Au NS with an ultraviolet−visible−NIR (UV−vis−NIR) spectrometer. Indicated as the black line in Figure S2, Au NR showed a transverse band (∼520 nm) in the visible and a longitudinal band (∼830 nm) in the near-infrared (NIR), respectively. Particularly, the NIR resonance peak showed ∼4 times higher intensity than the transverse band, which indicated a monodispersed colloidal Au NR product of high quality,[48] and this was also confirmed by the TEM images in Figure 1a. On the other hand, as the red line in Figure S2 shows, the LSPR resonance peak of Au NS is around 529 nm, and the sharp resonance peak suggested the uniform size distribution of Au NSs. Additionally, the high absorbance in the UV range (300−400 nm) indicates the interband transitions of electron oscillations.

The synthesized gold nanoparticles were subsequently developed into photothermal nanofilms with poly(vinylidene fluoride) (PVDF). We chose PVDF as the medium of the photothermal film due to its abundance, convenience during its molding and polymerization, as well as its high melting point (up to 170 °C) and stability after curing. As shown in Figure 1c, the nanocomposite was formed by mixing the synthesized gold nanoparticles with a PVDF polymer solution under magnetic stirring, and then, the nanofilm was formed by vacuum desiccation and oven baking (see Methods for experimental details). The resulting nanofilms are shown in Figure 1d1, d2. For both Au NR/PVDF and Au NS/PVDF nanofilms, with an increased weight concentration of loaded Au nanoparticles, the color of the nanofilm became darker. Calibrated with a ruler (Figure 1d3, d4), the diameter of the nanofilm was determined as ∼2.5 cm and the thickness was ∼0.05 mm.

The optical characterization of nanofilms was performed via UV−vis−NIR spectrometer measurement. The measured absorption spectrum is shown in Figure 2a,b. Both of the Au NR/PVDF and Au NS/PVDF nanofilms showed an intensified spectrum absorption with an increased Au loading weight concentration. Particularly, since the spectrum of the nanofilm was broad, especially for nanofilms with a small concentration of Au nanoparticles with a relatively low optical density, we determined the centered wavelengths of these nanofilms via a two-step fitting process. As shown in Figure S3a−e, we first

https://doi.org/10.1021/acsomega.2c01146
ACS Omega 2022, 7, 20750−20760

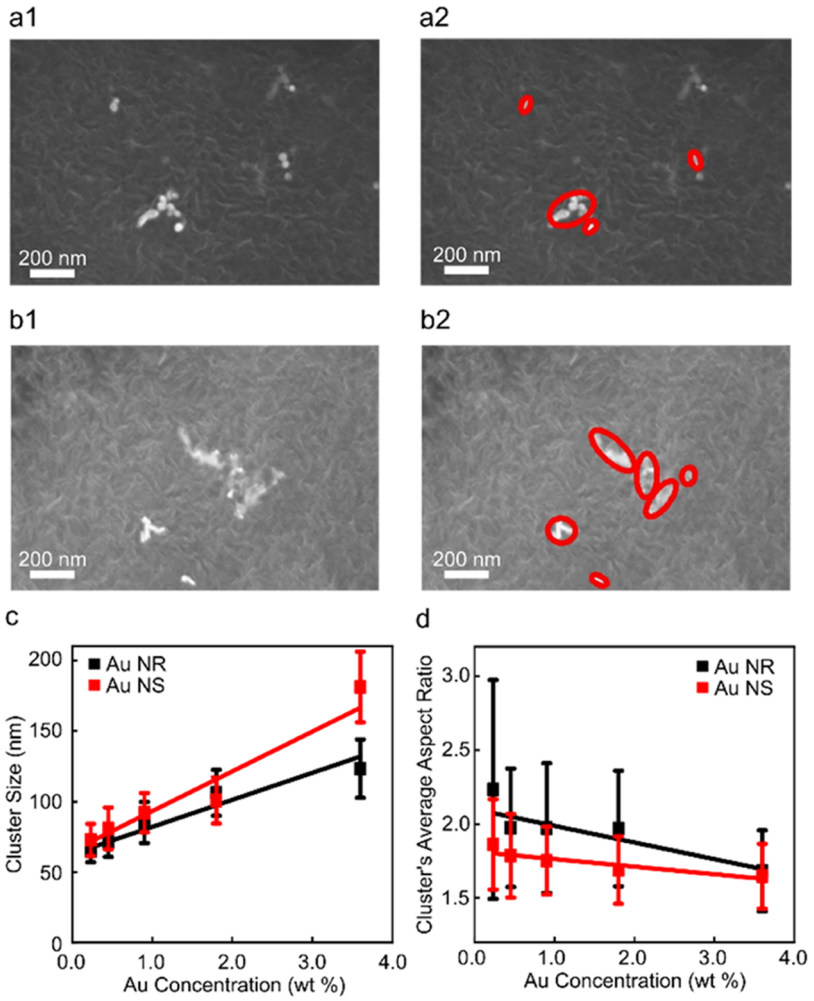

Figure 3. Morphological characterization of nanofilms. (a1, b1) Representative SEM images to show the Au NS/PVDF nanofilm, and the aggregated cluster marked by the programmed codes; (a2, b2) representative SEM images to show the Au NR/PVDF nanofilm, and the aggregated cluster marked by the programmed codes; (c) averaged sizes of aggregated clusters inside Au NS/PVDF and Au NR/PVDF nanofilms as a function of the Au loading weight percentage; and (d) averaged aspect ratios of aggregated clusters inside Au NS/PVDF and Au NR/PVDF nanofilms as a function of the Au loading weight percentage.

smoothed the absorbance spectrum of nanofilms via polynomial fitting (shown by the red line). Then, we fitted the absorption spectrum with multiple Gaussian peaks with a natural lifetime (σ = 0.05 of standard deviation) close to the peak width of monochromatic lasers. Then, based on these fitted Gaussian peaks (shown in green), we leveled the background of the spectrum by choosing those peaks with dramatic intensities ($I > 0.6I_{average}$) and rendered/described the rest of the prominent values into an approximate peak that has a mean centered wavelength (shown in orange).

As shown in Figure 2c, the Au NR/PVDF nanofilm showed spectral blue shifts from ~980 to ~580 nm as the Au loading concentration increased from 0.23 to 3.60%. However, the Au NS/PVDF nanofilm showed almost the same spectral peak with an increased Au loading concentration. The optical densities of Au NR/PVDF and Au NS/PVDF nanofilms are summarized in Figure 2d. Both Au NR/PVDF and Au NS/PVDF nanofilms exhibited an increased optical density (defined as the plasmonic peak intensity) with an increased Au loading concentration. Notably, the Au NS/PVDF nanofilm showed a higher optical density than the Au NR/PVDF nanofilm, while the Au NR/PVDF nanofilm had a wider light-receiving range than the Au NS/PVDF nanofilm. In other words, the nonlinear relationship between the optical density of the Au NR/PVDF nanofilm and the Au loading concentration, as well as the spectral blue shifts of the Au NR/PVDF nanofilm, suggested the existence of strong plasmonic coupling effects of the formed Au NR aggregations.

To observe the agglomerated clusters of Au nanoparticles in the nanofilm, we characterized the morphology of gold nanoparticles inside the PVDF nanofilm. We examined the gold nanoparticles' distribution via characterization of the sliced sample nanofilm with scanning electronic microscopy (SEM). The representative SEM images of Au NR/PVDF and Au NS/PVDF nanofilms are shown in Figure 3a1,b1. Other SEM images with varied distributions of gold nanoparticles in the nanofilm are shown in Figures S3 (Au NR/PVDF nanofilm) and S4 (Au NS/PVDF nanofilm), respectively. Specifically, Au NRs in the nanofilms were aggregated into clusters during solvent evaporation in the process of nanofilm fabrication, and both the number and size of agglomerations increased with the Au loading weight concentration. Similarly, Au NSs formed fewer agglomerations in the medium of PVDF than Au NRs given the same Au loading concentration.

To statistically analyze the formed clusters in the nanofilms, we processed the characterized SEM images with programmed

https://doi.org/10.1021/acsomega.2c01146
ACS Omega 2022, 7, 20750−20760

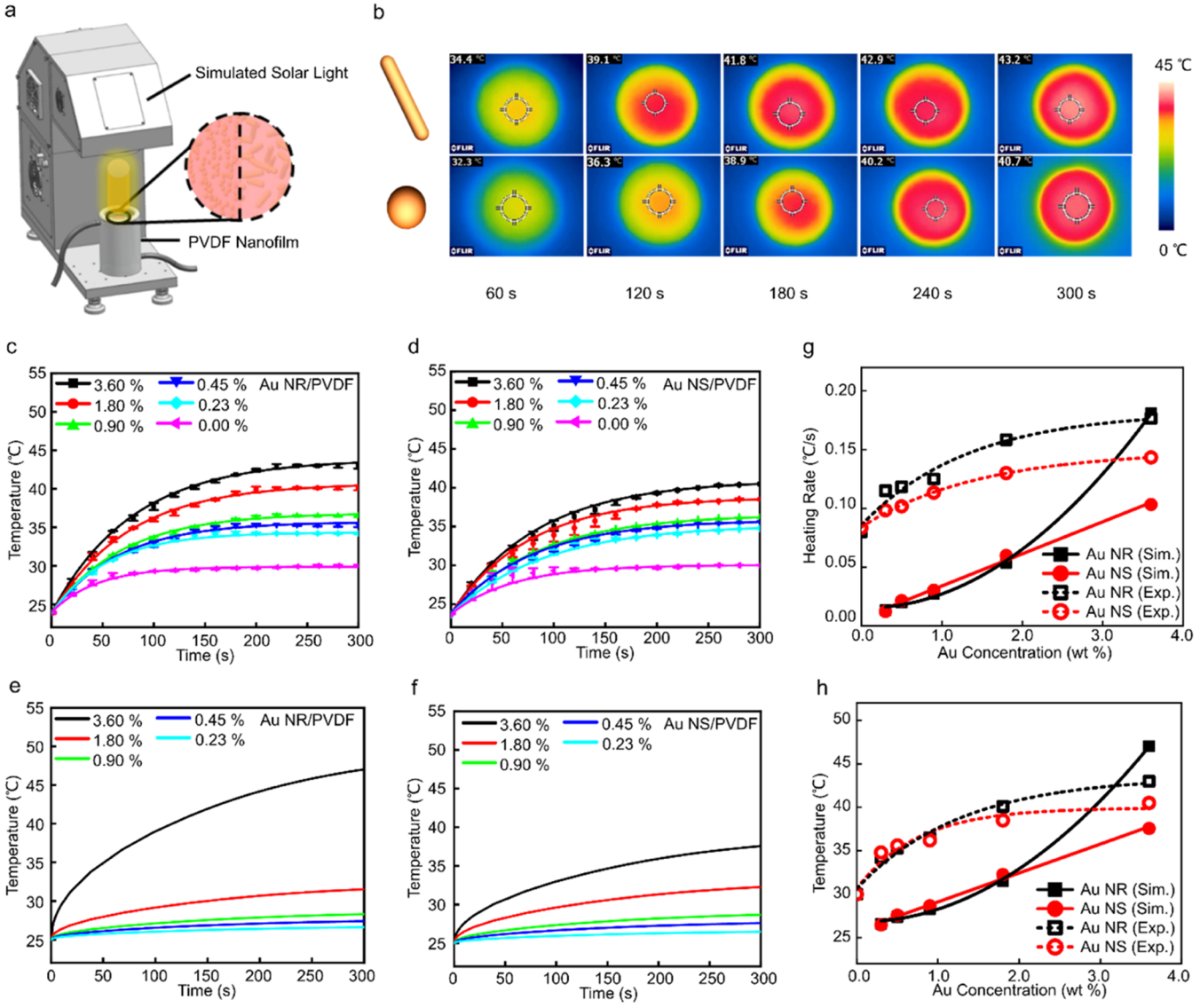

Figure 4. Solar photothermal performances of nanofilms. (a) Scheme depicts the solar photothermal experimental setup; (b) recorded thermal images of Au NR/PVDF (upper row) and Au NS/PVDF (lower row) nanofilms of different illumination times obtained by an infrared camera; (c, d) experimentally measured solar photothermal performances of Au NR/PVDF and Au NS/PVDF nanofilms as a function of time; (e, f) simulated solar photothermal performances of Au NR/PVDF and Au NS/PVDF nanofilms as a function of time; (g) experimental and simulated solar photothermal heating rates of Au NR/PVDF and Au NR/PVDF nanofilms as a function of loaded Au weight concentration; and (h) experimental and simulated equilibrium temperatures of Au NR/PVDF and Au NR/PVDF nanofilms as a function of loaded Au weight concentration.

codes for computational vision (CV) recognition (see Method for coding details). Figure 3a2,b2 shows the processed images originated from Figure 3a1,b1. The aggregated clusters were identified and approximated with elliptical fits. Marked in red, the size of a cluster was averaged by the longitudinal axis and transverse axis of fitted curves. The statistically counted size distributions are summarized in Figure 3c. For both Au NR/PVDF and Au NS/PVDF nanofilms, the size of formed clusters inside nanofilms increased linearly with the Au loading concentration, which confirmed our assumption mentioned above that the size of clusters increased with the Au loading concentration. It is intriguing that for Au NR/PVDF nanofilms, the size of the nanoclusters increased with Au NR loading concentrations, which led to the blue shifts of the centered wavelength, which is different from the cases of Au NS/PVDF nanofilms that slightly red-shift.[20,49] Therefore, we hypothesized that the decreased aspect ratio (that usually contributes to blue shifts[23,50]) outweighs the size effects (that contributes to red shifts) during the increased loading weight concentrations of Au NR/PVDF nanofilms.

Therefore, we summarized the aspect ratios of formed aggregated clusters in Au NR/PVDF and Au NS/PVDF nanofilms in Figure 3d. Specifically, the aspect ratio of formed clusters in Au NR/PVDF nanofilms decreased from ∼2.3 to ∼1.5, which suggested that the formed spherical clusters have resonance in the visible and high intensity that contribute to the spectral blue shifts and increased optical density of the Au NR/PVDF nanofilm in Figure 2c,d, respectively.

We assumed that the increased size of formed agglomerated clusters inside the nanofilm would lead to strong plasmonic coupling effects of clusters as well as improved photothermal performance; therefore, we evaluated the solar photothermal performance of Au NR/PVDF and Au NS/PVDF nanofilms to validate the assumption. As shown in Figure 4a, the nanofilms

https://doi.org/10.1021/acsomega.2c01146
ACS Omega 2022, 7, 20750−20760

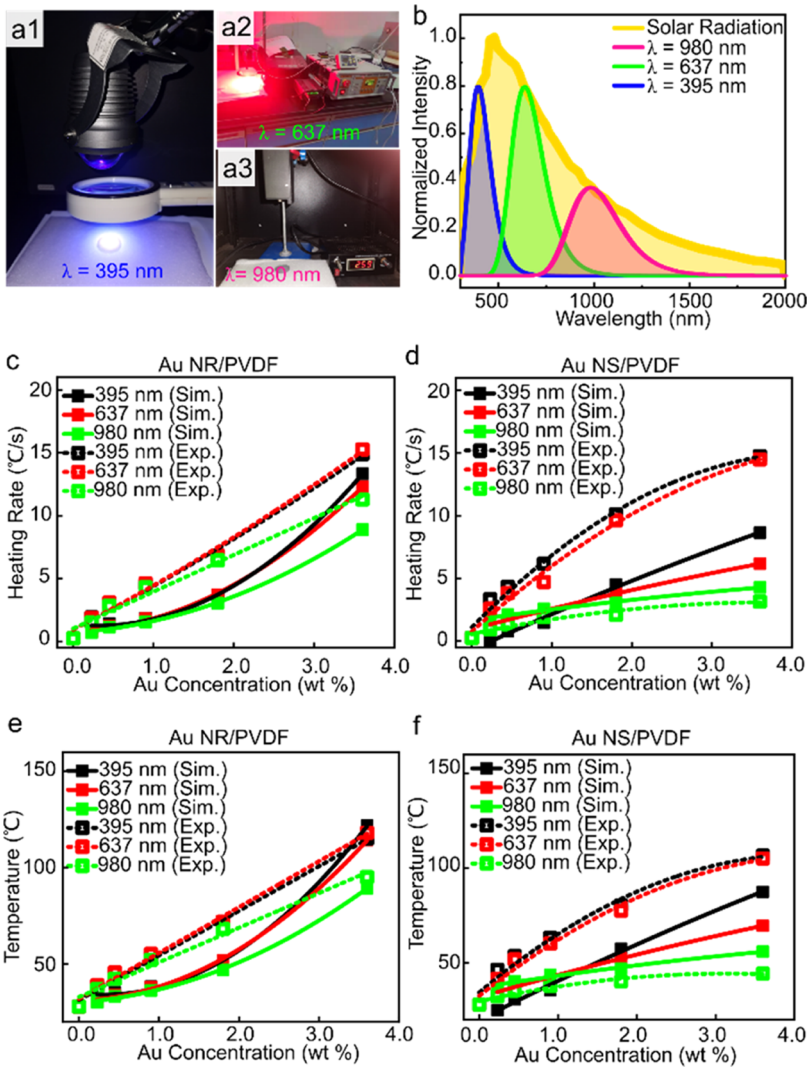

Figure 5. Monochromatic laser photothermal performance of nanofilms. (a) Photograph of monochromatic laser with centered wavelengths of 395 nm (a1), 637 nm (a2), and 980 nm (a3). (b) Solar spectrum and monochromatic laser spectrum. (c, d) Experimentally measured and calculated heating rates of Au NR/PVDF and Au NS/PVDF nanofilms as a function of time with illumination of different monochromatic lasers as a function of the Au weight concentration. (e, f) Experimentally measured and calculated equilibrium temperatures of Au NR/PVDF and Au NS/PVDF nanofilms as a function of time with illumination of different monochromatic lasers as a function of the Au weight concentration.

were illuminated by a simulated solar light source, and the temperature changes in the sample nanofilm were monitored by an infrared camera. Figure 4b shows the representative recorded thermal images of Au NR/PVDF and Au NS/PVDF nanofilms after receiving different times of solar illumination. Both of the nanofilms showed significantly elevated temperatures after ∼300 s. Experimentally measured solar photothermal performances of Au NR/PVDF and Au NS/PVDF nanofilms are summarized as a function of time in Figure 4c,d, respectively.

The measured solar photothermal heating rate and equilibrium temperature of Au NR/PVDF and Au NR/PVDF nanofilms are summarized as functions of the Au weight concentration in Figure 4g,h as dashed curves, respectively. As the weight percentage increased in the cell solution from 0 to 3.60%, the warming rate of Au NS/PVDF (red dashed curves) increased from 0.07 to 0.12 °C/s compared to that of Au NR/PVDF (black dashed curves) from 0.08 to 0.17 °C/s. Similarly, the temperature at equilibrium of Au NS/PVDF (red dashed curves) increased from 30 to 37 °C as the weight percentage in the nanofilm increased from 0 to 3.60%, compared to that of Au NR/PVDF (black dashed curves), which increased from 30 to 40 °C.

To further validate the plasmonic photothermal performance of nanofilms, we applied numerical simulation to model the photothermal effects. As shown in Figure S5, the simulation was performed with the two-dimensional (2D) heat transfer module of COMSOL Multiphysics to predict the temperature changes of the nanofilm under solar illumination (see Method for simulation details). The predicted temperature changes of Au NR/PVDF and Au NS/PVDF nanofilms in Figure 4e,f basically follow the trend of experimentally measured results in Figure 4c,d.

The simulated solar photothermal heating rate and equilibrium temperature of Au NR/PVDF and Au NR/PVDF nanofilms are also summarized in solid lines as a function of the Au weight concentration in Figure 4g,h, respectively. Both experimental and simulated results indicated that the Au NR/PVDF nanofilm outperformed the Au NS/PVDF nanofilm in terms of the photothermal heating rate and

https://doi.org/10.1021/acsomega.2c01146
ACS Omega 2022, 7, 20750−20760

temperature at equilibrium due to the stronger plasmonic coupling effects and photothermal performance of Au NR clusters in the nanofilm. It should be noticed that the simulated heating rate and temperature at equilibrium of the Au NR/PVDF nanofilm exhibited a nonlinear growth rate with increased Au loaded weight concentration, which differed from experimentally measured data where both the heating rate and the temperature at equilibrium's growth rate decreased and eventually saturated with increased Au loaded weight concentration. We attributed this deviation to the underestimation of the heat dissipation rate in the simulation model.

We further quantified each band's contribution during the solar photothermal performance via evaluating the warming rate with illumination of monochromatic UV, visible, and NIR lasers. As shown in Figure 5a1−a3, we performed laser photothermal warming by selecting a monochromatic light-emitting diode (LED) laser of UV (λ = 395 nm), visible (λ = 637 nm), and NIR (λ = 980 nm) as the light sources. The experimentally measured $T-t$ curves of Au NR/PVDF and Au NS/PVDF nanofilms are summarized in Figure S6a−c and d−f, respectively. Furthermore, we validated the heat transfer situation of nanofilms under monochromatic laser illumination through numerical simulation. The calculation was performed by describing monochromatic laser light sources of different wavelengths of 395, 637, and 980 nm approximately into Gaussian beams (Figure 5b). The simulation $T-t$ curves of Au NR/PVDF and Au NS/PVDF nanofilms are summarized in Figure S7a−c and d−f, which basically matched the experimentally measured results in Figure S6a−c and d−f.

The experimentally measured and simulated warming rates of different monochromatic lasers are summarized as a function of the loaded Au weight concentration in Figure 4c (Au NR/PVDF) and 4d (Au NS/PVDF), and the experimentally measured and simulated equilibrium temperatures of different monochromatic lasers are summarized as a function of the loaded Au weight concentration in Figure 4e (Au NR/PVDF) and 4f (Au NS/PVDF), respectively. The simulated results were in excellent agreement with the experimental value. UV and visible monochromatic lasers outperformed the NIR laser in both of the Au NR/PVDF and Au NS/PVDF nanofilm photothermal processes in terms of the heating rate and equilibrium temperature, which indicated that UV and visible bands contributed more than the NIR band in the process of solar photothermal performance. Notably, the Au NR/PVDF nanofilm exhibited a much more significantly higher heating rate and equilibrium temperature than the Au NS/PVDF nanofilm, which demonstrated that the aggregated Au NR clusters in the Au NR/PVDF nanofilm contributed to the boosted solar photothermal performance by extending the light-receiving range to the longer wavelength.

To further quantify the photothermal performance of Au NR/PVDF and Au NS/PVDF, we evaluated their light conversion efficiency, which was calculated by the energy balance function, and the light-to-heat conversion rate can be estimated as $\eta = E_{in}/E_0$, where $E_{in} = \Sigma m_i C_{p,i}(T_n - T_0)$ describes the absorbed energy by the Au NR/PVDF or Au NS/PVDF nanofilm and $E_0 = Pst$ describes the overall energy output provided by the light source (see the Methods section for a detailed information). The calculated light-to-heat conversion efficiencies of solar photothermal and monolaser photothermal are summarized in Tables S1 and S2, respectively.

As shown in Figure S1, as the loading weight of Au increased from 0.23 to 3.60%, both Au NR/PVDF and Au NS/PVDF nanofilms showed increased solar photothermal conversion efficiencies from ∼1.0 to 12.0%, although Au NR films showed a slightly higher conversion efficiency than Au NS films. Table S2 shows Au NR films and Au NS films under different illuminations of monolasers with wavelengths of 395, 637, and 980 nm. NR films showed an ∼10.0% higher photothermal conversion rate than Au NS films in all cases of monolaser illumination. This result is consistent with our observations and assumptions mentioned above that the aggregated Au NR clusters in the Au NR/PVDF nanofilm contributed to the boosted solar photothermal performance by extending the light-receiving range to the longer wavelength, and to some extent, it proved the Au NR/PVDF nanofilm's potential in utilizing safer and biofriendly IR light in natural solar light.

CONCLUSIONS

In this manuscript, we chemically synthesized Au NRs and developed them into Au NR/PVDF nanofilms. Through morphological examination and statistical analysis, we found the formed various styles of coupled Au NR clusters in the nanofilm, which contributed to the spectral blue shifts and boosted the photothermal performance. Particularly, through quantitative analysis of the nanofilm's composition, optical characteristics, and photothermal response under solar irradiation and/or under monochromatic laser illumination, we found that the as-synthesized Au NRs formed Au NR clusters, which significantly improved the solar energy conversion rate via extending the light harvesting range and the nanofilm's optical density. We believe our work has demonstrated that the Au NRs have huge potential for plasmonic solar photothermal applications and are promising for a vast range of applications, such as nanomedicine, cancer therapy, tumor imaging, solar harvesting, etc.

METHODS

Chemicals and Materials. Gold chloride hydrate, hydroquinone (AR), sodium borohydride (96%), and *N*,*N*-dimethylformamide (DMF, AR, 96%) were purchased from Aladdin. Hexadecyl trimethyl ammonium bromide (CTAB, AR), trisodium citrate dehydrate (AR), and poly(vinylidene fluoride) (PVDF, MW = 1 million) were purchased from the Sinopharm Chemical Reagent. Sodium hydroxide (AR) and silver nitrate solution was purchased from Macklin. Ultrapure water (18.2 MΩ·cm^{-1}) was produced by a Millipore water purification system.

Au Nanoparticle Synthesis. The synthesis method of Au NRs was applied as a seed-mediated growth technique developed by Leonid Vigderman et al.[51] The Au seeds were first prepared by fast reducing the Au precursor with sodium borohydride and were subsequently developed into Au NRs in the bath solution. Typically, 0.01 M sodium borohydride was dissolved in 0.01 M sodium hydroxide solution. Under rapid stirring, 0.46 mL of freshly prepared sodium borohydride solution was added into the $HAuCl_4$ solution (10 mL, 0.5 mM) in 0.1 M CTAB. The color of the solution changed from yellow to light brown, and then, it was used for the seed solution.

For Au NR growth, 1 mL of silver nitrate solution (0.1 M) was added into the $HAuCl_4$ solution (100 mL, 0.5 mM) with 0.1 M CTAB, and then, hydroquinone aqueous solution (5

https://doi.org/10.1021/acsomega.2c01146
ACS Omega 2022, 7, 20750−20760

mL, 0.1 M) was added. The solution was kept for stirring at 30 °C until completely clear; then, 1.5 mL of seed solution was added. The color of the growth solution gradually changed from colorless to wine-red. After aging overnight, the resulting Au NRs were finally obtained after being washed repeatedly by centrifugation and redispersed in water.

The synthesis of Au NSs was adopted from the Turkevich method,[52] which was to reduce the Au precursor with trisodium citrate under vigorous stirring and boiling. Typically, 50 mL of $HAuCl_4$ solution (10 mM) is heated to boiling in an oil bath at 137 °C. Under vigorous stirring, 1.5 mL of trisodium citrate aqueous solution (0.01 g/mL) was quickly added into the boiling $HAuCl_4$ solution. The color changed from light yellow to dark blue and then wine-red. The solution was kept refluxed for another 30 min and then washed with deionized water three times and finally redispersed in water.

Au Nanoparticle/PVDF Nanofilm Synthesis. PVDF powder and DMF solution were mixed in a beaker at a mass fraction ratio of 1:10. The beaker was sealed to prevent evaporation of DMF, and the mixture was magnetically stirred overnight to ensure complete dissolving of PVDF. After centrifugation of the gold nanoparticles, the pellets were redispersed in 100 μL of DMF with subsequent ultrasonication. Then, 1 mL of PVDF/DMF solution and 100 μL of Au/DMF were placed in a glass Petri dish. The solution was mixed via stirring, and excessive air bubbles were removed. The solution was placed in a vacuum drying oven at 60 °C to remove the DMF solvent to obtain dry Au/PVDF nanofilms. The resulting Au weight concentration in the nanofilm was quantitatively determined via an inductively coupled plasma-mass spectrometry (ICP-MS) study.

Nanofilm Optical Measurement. The optical responses of Au NR and Au NS colloidal solution and Au/PVDF nanofilms were characterized by the UV−vis−NIR spectrometer UV-3600 (SHIMADZU). The sample spectrum was recorded at the wavelength range of 400−1200 nm and a slit width of 2 nm. The recorded spectra were normalized and fitted by the Gaussian peak to determine the resonance peak and full width at half-maximum (FWHM).

Nanofilm Morphological Characterization. The morphology of the nanofilm characterization was performed with a field emission scanning electron microscope (FESEM, SU8020, HITACHI) with an acceleration voltage of 10 kV. The nanofilm was cut into thin slices with a thickness of ∼50 nm with an ultrathin nanoblade slicer for SEM examination.

Computational Vision Recognition. The obtained SEM images were processed by programmed Python CV codes to identify formed clusters (codes are available on https://github.com/MinXi2021/clusters_recognition_CV_codes.git). Typically, the images were first leveled at the threshold, and then, the formed clusters were identified via approximating with a polygon. The size of the cluster was averaged by the longitudinal axis and transverse axis of the fitted curves.

Photothermal Experiments. For solar photothermal experiments, Au/PVDF nanofilms with different concentrations of Au loaded weight concentrations were placed under a solar simulator (7IS0503A). The temperatures of nanofilms were recorded by an infrared thermal imaging camera (FLIR C2) every 20 s with an infrared camera until the temperature change leveled off. The light intensity of the solar simulator was adjusted to a solar constant (1367 ± 7 W/m^2) calibrated by an optical power meter.

For the study of the monochromatic laser photothermal experiment, the LED lasers with centered wavelengths of 395, 637, and 980 nm were applied, and the output irradiance power was adjusted to 1.8 W (with the spot of the illuminated area of ∼5 cm^2) calibrated by an optical power meter.

All measurements were performed thrice to check the reproducibility.

Solar Photothermal Simulations. The heat transfer module of COMSOL Multiphysics was used to calculate the photothermal response. As shown in Figure S5, the sample nanofilm (indicated in the blue meshed region at the bottom) was modeled, which is described as a cylinder with radius 1.25 cm and thickness 0.005 cm in the space of air. The input radiance was set perpendicular to the sample tube in the Z direction.

The partial differential equations eqs 1 and 2 were solved to calculate the temperature distribution of the system. eq 1 describes the thermal equilibrium of the overall system, where Q_r is the generated heat; and ρ_{air}, ρ_{PVDF}, C_{air}, and C_{PVDFn} are the densities and heat capacities of air and the solution, respectively.

$$\frac{\partial Q_r}{\partial t} = \rho_{air} C_{air} \frac{\partial T_{air}}{\partial t} + \rho_{PVDF} C_{PVDF} \frac{\partial T_{PVDF}}{\partial t} \tag{1}$$

eq 2 describes the photothermal process, where K_{PVDF} is the nanofilm's absorption coefficient and G is the radiation power density.

$$\frac{\partial Q_r}{\partial t} = K_{PVDF} G \tag{2}$$

For the calculation of the cell solution's heat transfer under solar light illumination, similar to our previous study,[19] we approximated and then processed the solar spectrum into a series of elemental beams, and each elemental beam was described by the Gaussian fit curve (eq 3) as

$$I_i = \frac{I_0}{\sqrt{2\pi}\sigma} e^{-(f-f_0)^2/2\sigma^2} \tag{3}$$

where I_i is each processed beam's intensity (the laser input power was set as 1300 W/m^2), I_0 is the corresponding intensity of the solar spectrum, f_0 is the central frequency of the beam, and σ is the standard deviation that is proportional to D_i (beam diameter of $1/e^2$ width) defined as $\sigma = \frac{D_i}{f_0}$, and we chose σ = 0.02 for simulation.

Therefore, the solar power intensity can be described as

$$G = \sum a_i \cdot I_i \tag{4}$$

where a_i is each approximated elemental Gaussian beam's portion of the overall solar irradiance power and I_i is the elemental beam's corresponding intensity to each frequency. The partial differential equation to be solved can be rewritten as eq 5

$$\frac{\partial Q_r}{\partial t} = \sum \kappa_i \cdot a_i \cdot I_i = \rho_{air} C_{air} \frac{\partial T_{air}}{\partial t} + \rho_{PVDF} C_{PVDF} \frac{\partial T_{PVDF}}{\partial t} \tag{5}$$

where a_i can be calculated from the measured optical density of the nanofilm from eq 6 as

$$a_i = \sum \kappa_i \tag{6}$$

https://doi.org/10.1021/acsomega.2c01146
ACS Omega 2022, 7, 20750−20760

where the absorption coefficient is described as the sum of κ_i, which is the optical density at each frequency.

The model was meshed into ∼3000 elements, and the simulation was performed with the PARSIDO time-dependent solver to reach the relative tolerance of 0.01.

For the heat transfer simulation, monochromatic laser illumination and monochromatic laser light sources with centered wavelengths of 395, 637, and 980 nm were approximately described as Gaussian beams. Since σ of the monochromatic laser beam is usually larger than 0.02, we chose $\sigma = 0.02$ to describe the laser intensity with a Gaussian fit. The laser input power was set as 18 000 W/m^2.

Photothermal Conversion Efficiency Calculation. The photothermal conversion efficiency under simulated solar irradiation can be obtained from the following equation

$$\eta = \sum m_i C_{p,i}(T_n - T_0)/Pst \tag{7}$$

where m_i and $C_{p,i}$ are the mass ($m_{Au/PVDF}$ ∼0.2 g) and heat capacity ($C_{p,Au}$ = 0.13 J g^{-1} K^{-1}, $C_{p,PVDF}$ = 1.17 J g^{-1} K^{-1}) of Au and PVDF, respectively; T_n is the highest temperature; T_0 is the initial temperature; P is the solar irradiation power (∼1300 W m^{-2}); s is the film area (∼6 cm^2); and t is the irradiation time.

The photothermal conversion efficiency of Au/PVDF films under laser irradiation was calculated by the energy balance function.

$$\sum m_i C_{p,i}\frac{dT}{dt} = Q_{in} - Q_{ext} \tag{8}$$

where T is the temperature, Q_{in} is the heat absorbed by the Au/PVDF film, and Q_{ext} is the heat dissipated by the surroundings.

$$Q_{in} = I \cdot A_{abs} \cdot \eta \tag{9}$$

where I is the laser power, A_{abs} is the absorbance, and η is the photothermal conversion efficiency.

$$Q_{ext} = hs(T_n - T_0) \tag{10}$$

where h is the heat transfer coefficient.

By fitting the temperature vs time curve after turning off the laser

$$T(t) = T_0 + (T_n - T_0)\exp(-Bt) \tag{11}$$

where $B = \frac{hs}{\sum m_i C_i}$, when the temperature is constant under the laser, $\frac{dT}{dt} = 0$ and $Q_{in} = Q_{ext}$, from which the photothermal conversion efficiency can be obtained as follows

$$\eta = \frac{hs(T_n - T_0)}{I \cdot A_{abs}} \tag{12}$$

■ ASSOCIATED CONTENT

Supporting Information

The Supporting Information is available free of charge at https://pubs.acs.org/doi/10.1021/acsomega.2c01146.

Size distribution analysis; SEM images of nanofilms; experimentally measured and simulated UV−vis−NIR spectrum and other information (PDF)

■ AUTHOR INFORMATION

Corresponding Authors

Jixiang Zhang − *School of Mechatronics & Vehicle Engineering, Chongqing Jiaotong University, Chongqing 400074, P. R. China; Institute of Solid State Physics and Key Laboratory of Photovoltaic and Energy Conservation Materials, Hefei Institutes of Physical Science, Chinese Academy of Sciences, Hefei, Anhui 230031, P. R. China;* Email: zhangjx@cqjtu.edu.cn

Zhenyang Wang − *Institute of Solid State Physics and Key Laboratory of Photovoltaic and Energy Conservation Materials, Hefei Institutes of Physical Science, Chinese Academy of Sciences, Hefei, Anhui 230031, P. R. China;* orcid.org/0000-0002-0194-3786; Email: zywang@iim.ac.cn

Min Xi − *Institute of Solid State Physics and Key Laboratory of Photovoltaic and Energy Conservation Materials, Hefei Institutes of Physical Science, Chinese Academy of Sciences, Hefei, Anhui 230031, P. R. China; The Key Laboratory Functional Molecular Solids Ministry of Education, Anhui Normal University, Wuhu, Anhui 241002, P. R. China;* orcid.org/0000-0003-4414-3110; Email: minxi@issp.ac.cn

Authors

Shenyi Ding − *School of Mechatronics & Vehicle Engineering, Chongqing Jiaotong University, Chongqing 400074, P. R. China; Institute of Solid State Physics and Key Laboratory of Photovoltaic and Energy Conservation Materials, Hefei Institutes of Physical Science, Chinese Academy of Sciences, Hefei, Anhui 230031, P. R. China;* orcid.org/0000-0002-6967-9790

Cui Liu − *Institute of Solid State Physics and Key Laboratory of Photovoltaic and Energy Conservation Materials, Hefei Institutes of Physical Science, Chinese Academy of Sciences, Hefei, Anhui 230031, P. R. China*

Nian Li − *Institute of Solid State Physics and Key Laboratory of Photovoltaic and Energy Conservation Materials, Hefei Institutes of Physical Science, Chinese Academy of Sciences, Hefei, Anhui 230031, P. R. China*

Shudong Zhang − *Institute of Solid State Physics and Key Laboratory of Photovoltaic and Energy Conservation Materials, Hefei Institutes of Physical Science, Chinese Academy of Sciences, Hefei, Anhui 230031, P. R. China;* orcid.org/0000-0002-0215-1641

Complete contact information is available at: https://pubs.acs.org/10.1021/acsomega.2c01146

Author Contributions

S.D. synthesized and characterized the Au NS and Au NR nanoparticles, performed the photothermal experiment, and took photographs of the experimental equipment (in Figures 1 and 5). Dr. M.X. designed the experiment, performed the simulation, analyzed the data, and wrote the manuscript. Dr. C.L., Dr. N.L., Dr. S.Z., Dr. J.Z., and Dr. Z.W. provided the lab equipment and funding support.

Notes

The authors declare no competing financial interest.

■ ACKNOWLEDGMENTS

The authors would like to acknowledge the financial support from the National Key Research and Development Project

https://doi.org/10.1021/acsomega.2c01146
ACS Omega 2022, 7, 20750−20760

(2020YFA0210703), the Key Laboratory Functional Molecular Solids, Ministry of Education (FMS202002), the National Natural Science Foundation of China (Nos. U2032159, U2032158, and 62005292), the Major Scientific and Technological Special Project of Anhui Province (202103a05020192), the Key Research and Development Program of Anhui Province (202104a05020036), the special fund project for local science and technology development guided by the central government of Anhui Province (202107d08050016), the Chongqing Municipal Key Project of Technological Innovation and Application Development (Lu-Chongqing Science and Technology Collaboration Project, cstc2020jscx-lyggX0007), the Chongqing Postgraduate Mentor Team Construction Project (JDDSTD2019007), the Chongqing Postgraduate Joint Training Base Project (JDLHPYJD2020032), the Collaborative Innovation Program of Hefei Science Center, CAS (2020HSC-CIP003), the Major Scientific and the CASHIPS Director's Fund (YZJJZX202015), and the technological Innovation Projects of Shandong Province (2019JZZY020243).

REFERENCES

(1) Cao, S.; Jiang, Q.; Wu, X.; Ghim, D.; Derami, H. G.; Chou, P. I.; Jun, Y. S.; Singamaneni, S. Advances in Solar Evaporator Materials for Freshwater Generation. *J. Mater. Chem. A* **2019**, *7*, 24092−24123.

(2) Wu, S.-L.; Chen, H.; Wang, H.-L.; Chen, X.; Yang, H.-C.; Darling, S. B. Solar-Driven Evaporators for Water Treatment: Challenges and Opportunities. *Environ. Sci.: Water Res. Technol.* **2021**, *7*, 24−39.

(3) Zhang, C.; Liang, H. Q.; Xu, Z. K.; Wang, Z. Harnessing Solar-Driven Photothermal Effect toward the Water−Energy Nexus. *Adv. Sci.* **2019**, *6*, No. 1900883.

(4) Eustis, S.; El-Sayed, M. A. Why Gold Nanoparticles Are More Precious than Pretty Gold: Noble Metal Surface Plasmon Resonance and Its Enhancement of the Radiative and Nonradiative Properties of Nanocrystals of Different Shapes. *Chem. Soc. Rev.* **2006**, *35*, 209−217.

(5) Baffou, G.; Quidant, R. Thermo-Plasmonics: Using Metallic Nanostructures as Nano-Sources of Heat. *Laser Photonics Rev.* **2013**, *7*, 171−187.

(6) Yeshchenko, O. A.; Bondarchuk, I. S.; Gurin, V. S.; Dmitruk, I. M.; Kotko, A. V. Temperature Dependence of the Surface Plasmon Resonance in Gold Nanoparticles. *Surf. Sci.* **2013**, *608*, 275−281.

(7) Gao, M.; Peh, C. K.; Phan, H. T.; Zhu, L.; Ho, G. W. Solar Absorber Gel: Localized Macro-Nano Heat Channeling for Efficient Plasmonic Au Nanoflowers Photothermic Vaporization and Triboelectric Generation. *Adv. Energy Mater.* **2018**, *8*, No. 1800711.

(8) Nazari, M.; Xi, M.; Lerch, S.; Alizadeh, M. H.; Ettinger, C.; Akiyama, H.; Gillespie, C.; Gummuluru, S.; Erramilli, S.; Reinhard, B. M. Plasmonic Enhancement of Selective Photonic Virus Inactivation. *Sci. Rep.* **2017**, *7*, No. 11951.

(9) Nazari, M.; Xi, M.; Aronson, M.; Mcrae, O.; Hong, M. K.; Gummuluru, S.; Sgro, A. E.; Bird, J. C.; Ziegler, L. D.; Gillespie, C.; Souza, K.; Nguyen, N.; Smith, R. M.; Silva, E.; Miura, A.; Erramilli, S.; Reinhard, B. M. Plasmon-Enhanced Pan-Microbial Pathogen Inactivation in the Cavitation Regime: Selectivity without Targeting. *ACS Appl. Nano Mater.* **2019**, *2*, 2548−2558.

(10) Jaque, D.; Maestro, L. M.; del Rosal, B.; Haro-Gonzalez, P.; Benayas, A.; Plaza, J. L.; Rodríguez, E. M.; Solé, J. G. Nanoparticles for Photothermal Therapies. *Nanoscale* **2014**, *6*, 9494−9530.

(11) Boyer, D.; Tamarat, P.; Maali, A.; Lounis, B.; Orrit, M. Photothermal Imaging of Nanometer-Sized Metal Particles among Scatterers. *Science* **2002**, *297*, 1160−1163.

(12) Hong, Y.; Reinhard, B. M. Optoplasmonics: Basic Principles and Applications. *J. Opt.* **2019**, *21*, No. 113001.

(13) Zhang, C.; Jia, F.; Li, Z.; Huang, X.; Lu, G. Plasmon-Generated Hot Holes for Chemical Reactions. *Nano Res.* **2020**, *13*, 3183−3197.

(14) Zhang, Y.; He, S.; Guo, W.; Hu, Y.; Huang, J.; Mulcahy, J. R.; Wei, W. D. Surface-Plasmon-Driven Hot Electron Photochemistry. *Chem. Rev.* **2018**, *118*, 2927−2954.

(15) Roller, E.-M.; Besteiro, L.; Pupp, C.; Khorashad, L.; Govorov, A.; Liedl, T. Hotspot-Mediated Non-Dissipative and Ultrafast Plasmon Passage. *Nat. Phys.* **2017**, *13*, 761−765.

(16) Liang, J.; Liu, H.; Yu, J.; Zhou, L.; Zhu, J. Plasmon-Enhanced Solar Vapor Generation. *Nanophotonics* **2019**, *8*, 771−786.

(17) Zhuang, T. T.; Liu, Y.; Li, Y.; Zhao, Y.; Wu, L.; Jiang, J.; Yu, S. H. Integration of Semiconducting Sulfides for Full-Spectrum Solar Energy Absorption and Efficient Charge Separation. *Angew. Chem., Int. Ed.* **2016**, *55*, 6396−6400.

(18) Li, Y.; Lin, C.; Wu, Z.; Chen, Z.; Chi, C.; Cao, F.; Mei, D.; Yan, H.; Tso, C. Y.; Chao, C. Y. H.; Huang, B. Solution-Processed All-Ceramic Plasmonic Metamaterials for Efficient Solar−Thermal Conversion over 100−727 °C. *Adv. Mater.* **2021**, *33*, No. 2005074.

(19) Xi, M.; Xu, L.; Li, N.; Zhang, S.; Wang, Z. Plasmonic $Cu_{27}S_{24}$ Nanocages for Novel Solar Photothermal Nanoink and Nanofilm. *Nano Res.* **2022**, *15*, 3161−3169.

(20) Xi, M.; Reinhard, B. M. Localized Surface Plasmon Coupling between Mid-IR-Resonant ITO Nanocrystals. *J. Phys. Chem. C* **2018**, *122*, 5698−5704.

(21) Zhuo, X.; Yip, H.-K.; Ruan, Q.; Zhang, T.; Zhu, X.; Wang, J.; Lin, H.; Xu, J.; Yang, Z. Broadside Nanoantennas Made of Single Silver. *ACS Nano* **2018**, *12*, 1720−1731.

(22) Zhuo, X.; Yip, H. K.; Cui, X.; et al. Colour Routing with Single Silver Nanorods. *Light: Sci. Appl.* **2019**, *8*, No. 39.

(23) Xi, M.; Reinhard, B. M. Evolution of Near- and Far-Field Optical Properties of Au Bipyramids upon Epitaxial Deposition of Ag. *Nanoscale* **2020**, *12*, 5402−5411.

(24) Liz-Marzán, L. M. Tailoring Surface Plasmons through the Morphology and Assembly of Metal Nanoparticles. *Langmuir* **2006**, *22*, 32−41.

(25) Burrows, N. D.; Lin, W.; Hinman, J.; Dennison, J.; Vartanian, A.; Abadeer, N.; Grzincic, E.; Jacob, L.; Li, J.; Murphy, C. Surface Chemistry of Gold Nanorods. *Langmuir* **2016**, *32*, 9905−9921.

(26) Wu, L.; Reinhard, B. M. Probing Subdiffraction Limit Separations with Plasmon Coupling Microscopy: Concepts and Applications. *Chem. Soc. Rev.* **2014**, *43*, 3884−3897.

(27) Nordlander, P.; Oubre, C.; Prodan, E.; Li, K.; Stockman, M. I. Plasmon Hybridization in Nanoparticle Dimers. *Nano Lett.* **2004**, *4*, 899−903.

(28) Jain, P. K.; Huang, W.; El-Sayed, M. A. On the Universal Scaling Behavior of the Distance Decay of Plasmon Coupling in Metal Nanoparticle Pairs: A Plasmon Ruler Equation. *Nano Lett.* **2007**, *7*, 2080−2088.

(29) Harris, N.; Arnold, M. D.; Blaber, M. G.; Ford, M. J. Plasmonic Resonances of Closely Coupled Gold Nanosphere Chains. *J. Phys. Chem. C* **2009**, *113*, 2784−2791.

(30) Chen, T.; Pourmand, M.; Feizpour, A.; Cushman, B.; Reinhard, B. M. Tailoring Plasmon Coupling in Self-Assembled One-Dimensional Au Nanoparticle Chains through Simultaneous Control of Size and Gap Separation. *J. Phys. Chem. Lett.* **2013**, *4*, 2147−2152.

(31) Yan, B.; Thubagere, A.; Premasiri, W. R.; Ziegler, L.; Negro, L. D.; Reinhard, B. Engineered SERS Substrates with Multiscale Signal Enhancement: Nanoparticle Cluster Arrays. *ACS Nano* **2009**, *3*, 1190−1202.

(32) Hong, Y.; Ahn, W.; Boriskina, S.; Zhao, X.; Reinhard, B. Directed Assembly of Optoplasmonic Hybrid Materials with Tunable Photonic−Plasmonic Properties. *J. Phys. Chem. Lett.* **2015**, *6*, 2056−2064.

(33) Chen, M.; He, Y.; Zhu, J. Quantifying and Comparing the Near-Field Enhancement, Photothermal Conversion, and Local Heating Performance of Plasmonic SiO_2@Au Core-Shell Nanoparticles. *Plasmonics* **2019**, *14*, 1019−1027.

(34) Bae, K.; Kang, G.; Cho, S. K.; Park, W.; Kim, K.; Padilla, W. J. Flexible Thin-Film Black Gold Membranes with Ultrabroadband Plasmonic Nanofocusing for Efficient Solar Vapour Generation. *Nat. Commun.* **2015**, *6*, No. 10103.

https://doi.org/10.1021/acsomega.2c01146
ACS Omega 2022, 7, 20750−20760

(35) Chen, M.; Wu, Y.; Song, W.; Mo, Y.; Lin, X.; He, Q.; Guo, B. Plasmonic Nanoparticle-Embedded Poly(p-Phenylene Benzobisoxazole) Nanofibrous Composite Films for Solar Steam Generation. *Nanoscale* **2018**, *10*, 6186−6193.
(36) Malachosky, E. W.; Guyot-Sionnest, P. Gold Bipyramid Nanoparticle Dimers. *J. Phys. Chem. C* **2014**, *118*, 6405−6412.
(37) Slaughter, L. S.; Wu, Y.; Willingham, B.; Nordlander, P.; Link, S. Effects of Symmetry Breaking and Conductive Contact on the Plasmon Coupling in Gold Nanorod Dimers. *ACS Nano* **2010**, *4*, 4657−4666.
(38) Willets, K. A.; Van Duyne, R. P. Localized Surface Plasmon Resonance Spectroscopy and Sensing. *Annu. Rev. Phys. Chem.* **2007**, *58*, 267−297.
(39) Brown, L. V.; Yang, X.; Zhao, K.; Zheng, B.; Nordlander, P.; Halas, N. Fan-Shaped Gold Nanoantennas Above Reflective Substrates for Surface-Enhanced Infrared Absorption (SEIRA). *Nano Lett.* **2015**, *15*, 1272−1280.
(40) Bauch, M.; Toma, K.; Toma, M.; Zhang, Q.; Dostalek, J. Plasmon-Enhanced Fluorescence Biosensors: A Review. *Plasmonics* **2014**, *9*, 781−799.
(41) Li, J. F.; Li, C. Y.; Aroca, R. F. Plasmon-Enhanced Fluorescence Spectroscopy. *Chem. Soc. Rev.* **2017**, *46*, 3962−3979.
(42) Felix-Rendon, U.; Berini, P.; De Leon, I. Ultrasensitive Nanoplasmonic Biosensor Based on Interferometric Excitation of Multipolar Plasmonic Modes. *Opt. Express* **2021**, *29*, 17365−17374.
(43) Aubry, A.; Lei, D. Y.; Maier, S. A.; Pendry, J. Interaction Between Plasmonic Nanoparticles Revisited with Transformation Optics. *Phys. Rev. Lett.* **2010**, *105*, No. 233901.
(44) Liu, N.; Weiss, T.; Mesch, M.; Langguth, L.; Eigenthaler, U.; Hirscher, M.; Sönnichsen, C.; Giessen, H. Planar Metamaterial Analogue of Electromagnetically Induced Transparency for Plasmonic Sensing. *Nano Lett.* **2010**, *10*, 1103−1107.
(45) Yang, Z.-J.; Zhang, Z.-S.; Zhang, L.-H.; Li, Q.-Q.; Hao, Z.; Wang, Q. Fano Resonances in Dipole-Quadrupole Plasmon Coupling Nanorod Dimers. *Opt. Lett.* **2011**, *36*, 1542−1544.
(46) Zhang, S.; Geryak, R.; Geldmeier, J.; Kim, S.; Tsukruk, V. V. Synthesis, Assembly, and Applications of Hybrid Nanostructures for Biosensing. *Chem. Rev.* **2017**, *117*, 12942−13038.
(47) Liu, R.; Jiang, L.; Liu, G.; Chen, G.; Li, J.; Liu, J.; Wang, X. Optical Response Properties of Stable and Controllable Au Nanorod. *J. Phys. Chem. C* **2019**, *123*, 13892−13899.
(48) Li, Q.; Zhuo, X.; Li, S.; Ruan, Q.; Xu, Q. H.; Wang, J. Production of Monodisperse Gold Nanobipyramids with Number Percentages Approaching 100% and Evaluation of Their Plasmonic Properties. *Adv. Opt. Mater.* **2015**, *3*, 801−812.
(49) He, D.; Hu, B.; Yao, Q.; Wang, K.; Yu, S. Large-Scale Synthesis of Flexible Free-Sensitivity: Electrospun PVA Nanofibers of Silver Nanoparticles. *ACS Nano* **2009**, *3*, 3993−4002.
(50) Zhu, X. Z.; Zhuo, X.; Li, Q.; Yang, Z.; Wang, J. F. Gold Nanobipyramid-Supported Silver Nanostructures with Narrow Plasmon Linewidths and Improved Chemical Stability. *Adv. Funct. Mater.* **2016**, *26*, 341−352.
(51) Vigderman, L.; Zubarev, E. High-Yield Synthesis of Gold Nanorods with Longitudinal SPR Peak Greater than 1200 Nm Using Hydroquinone as a Reducing Agent. *Chem. Mater.* **2013**, *25*, 1450−1457.
(52) Ding, W.; Zhang, P.; Li, Y.; Xia, H.; Wang, D.; Tao, X. Effect of Latent Heat in Boiling Water on the Synthesis of Gold Nanoparticles of Different Sizes by Using the Turkevich Method. *ChemPhysChem* **2015**, *16*, 447−454.

https://doi.org/10.1021/acsomega.2c01146
ACS Omega 2022, 7, 20750−20760